

Dynamical simulations of carotenoid photoexcited states using density matrix renormalization group techniques

Dilhan Manawadu,^{*,†,‡} Darren J. Valentine,^{†,¶} and William Barford^{*,†}

[†]*Department of Chemistry, Physical and Theoretical Chemistry Laboratory,
University of Oxford, Oxford, OX1 3QZ, United Kingdom*

[‡]*Linacre College, University of Oxford, Oxford, OX1 3JA, United Kingdom*

[¶]*Balliol College, University of Oxford, Oxford, OX1 3BJ, United Kingdom*

E-mail: dilhan.manawadu@chem.ox.ac.uk; william.barford@chem.ox.ac.uk

Abstract

We present a dynamical simulation scheme to model the highly correlated excited state dynamics of linear polyenes. We apply it to investigate the internal conversion processes of carotenoids following their photoexcitation. We use the extended Hubbard-Peierls model, \hat{H}_{UVP} , to describe the π -electronic system coupled to nuclear degrees of freedom. This is supplemented by a Hamiltonian, \hat{H}_ϵ , that explicitly breaks both the particle-hole and two-fold rotation symmetries of idealized carotenoid structures. The electronic degrees of freedom are treated quantum mechanically by solving the time-dependent Schrödinger equation using the adaptive time-dependent DMRG (tDMRG) method, while nuclear dynamics are treated via the Ehrenfest equations of motion. By defining adiabatic excited states as the eigenstates of the full Hamiltonian, $\hat{H} = \hat{H}_{\text{UVP}} + \hat{H}_\epsilon$, and diabatic excited states as eigenstates of \hat{H}_{UVP} , we present a computational framework to monitor the internal conversion process from the initial

photoexcited $1^1B_u^+$ state to the singlet triplet-pair states of carotenoids. We further incorporate Lanczos-DMRG to the tDMRG-Ehrenfest method to calculate transient absorption spectra from the evolving photoexcited state. We describe in detail the accuracy and convergence criteria for DMRG, and show that this method accurately describes the dynamical processes of carotenoid excited states. We also discuss the effect of the symmetry breaking term, \hat{H}_ϵ , on the internal conversion process, and show that its effect on the extent of internal conversion can be described by a Landau-Zener-type transition. This methodological paper is a companion to our more explanatory discussion of carotenoid excited state dynamics in, *Photoexcited state dynamics and singlet fission in carotenoids*, D. Manawadu, T. N. Georges and W. Barford, *J. Phys. Chem. A* (2023).

1 Introduction

Theoretical studies of the exotic nature of polyene excited states were pioneered by a seminal paper from Schulten and Karplus, which described the experimentally observed low-lying dark excited state of polyenes.^{1,2} They described the conjugated π -electron system using the semi-empirical Pariser-Parr-Pople (PPP) Hamiltonian³ and the configuration interaction (CI) method description of the wavefunction with double excitations. Their work was followed by several studies based on semi-empirical Hamiltonians, which helped formulate the theoretical understanding of polyene excited states.^{4–10}

Early *ab-initio* calculations of polyene excited states were based on self consistent field (SCF) and CI calculations.^{11,12} Improvements to the ground and excited state geometries of polyenes were brought about by the use of multiconfiguration self consistent field (MCSCF) method.¹³ Serrano-Andres and coworkers introduced the second order perturbation theory method CASPT2 with a complete active space SCF (CASSCF) wavefunction as the reference state to study electronic states of polyenes.¹⁴ Their calculation provided first evidence from an *ab-initio* study for the existence of a dark low-lying polyene excited state. More recently, time-dependent density functional theory (TD-DFT),^{15,16} extended algebraic diagrammatic construction (extended-ADC(2)),¹⁷ CASSCF with n -electron valence perturbation theory (NEVPT),¹⁸ and density functional theory with multireference configuration interaction^{19,20} have been utilized to study polyene excited states. However, application of complete active space methods to model long chain polyene systems is challenging because of the exponential growth of the many-body Hilbert space with the size of the single particle basis.

In 1992, White introduced the density matrix renormalization group (DMRG) algorithm to study strongly correlated quantum lattice systems.²¹ DMRG was quickly adapted to study polyene photophysics, as applied to one-dimensional systems it yields quasi-exact results for a finite-size Hilbert space.^{22–27} DMRG was first utilized to model *ab-initio* Hamiltonians in 1999.²⁸ Ghosh et al. demonstrated that the CASSCF method can be incorporated to a DMRG algorithm, allowing for modelling polyene systems of natural carotenoid lengths.²⁹

While the inherent multireference nature of DMRG accounts for static correlations, perturbative theory corrections are required to accurately describe the dynamic correlations present in the system.^{30,31} More recent *ab-initio* studies on polyene excited states using multireference perturbation theory (MPRT) DMRG, which accounts for the dynamic correlations have reignited the debate on carotenoid excited state energy ordering.^{32,33}

The original DMRG formulation of White has been extended to form a family of time-dependent DMRG (TD-DMRG) algorithms, designed to model time dependent phenomena of molecular systems. One of the widely used TD-DMRG algorithms is the adaptive time-dependent DMRG (tDMRG) algorithm, independently developed by Daley et al.,³⁴ and White and Feiguin³⁵ to study time evolution of weakly entangled systems. Examples of applications of adaptive tDMRG in molecular physics include modelling magnetization transport in spin- $\frac{1}{2}$ chains,³⁶ demonstrating spin-charge separation in cold Fermi gases,³⁷ calculating zero temperature conductance of strongly correlated nanostructures,³⁸ elucidating transport properties of quantum-dot systems connected to metallic leads,³⁹ evaluating spectral functions of spin-1 Heisenberg antiferromagnetic chain,⁴⁰ exciton transport in one-dimensional Hubbard insulators,⁴¹ and non-equilibrium transport in single-impurity Anderson model.⁴² Techniques based on tensor network models have recently been used to study dynamics of photophysical systems, for example, ultrafast relaxation and localization of photoexcited states in light emitting polymers,^{43–45} internal conversion in pyrazine,⁴⁶ and singlet fission in substituted pentacene dimers.⁴⁷ Readers are referred to a recent review by Ren and co-workers on applications of different TD-DMRG algorithms to model dynamics of quantum systems.⁴⁸

While state-of-the-art *ab-initio* methods have had great success in calculating static properties of polyene excited states, due to computational expediences the use of semi-empirical Hamiltonians with a single electron basis is more attractive to model dynamical processes of photoexcited polyenes. With the correct parametrization DMRG has been shown to work very well for semi-empirical Hamiltonians with a reduced single-particle basis.^{49,50} The

DMRG algorithm with the PPP Hamiltonian has been widely used to study the electronic properties of conjugated polyenes.^{23–26,51–53}

Recently, the present authors developed DMRG methods to simulate internal conversion of photoexcited states and singlet triplet-pair production in carotenoid systems of up to 22 conjugated carbon atoms. Carotenoids are particularly challenging, as they exhibit strong electronic correlation and strong electron-nuclear coupling. In dimers, they also exhibit singlet fission after photoexcitation. In ref 54 we implemented mixed quantum-classical dynamics, treating the electrons via adaptive tDMRG and the nuclei via Ehrenfest dynamics, to simulate internal conversion in zeaxanthin. In a companion paper⁵⁵ we extend those simulations to neurosporene and we also describe our calculations of transient absorption.

The primary purpose of this paper is to describe in more detail the methodology of the tDMRG-Ehrenfest simulation for a wider theoretical chemistry community. In particular, we emphasize that tDMRG is a rather natural generalization of the finite-lattice algorithm of static DMRG. We also explain the Lanczos-DMRG method for computing the transient absorption spectrum of the time-evolving photoexcited state. We show that DMRG methods can accurately and reliably describe the complex photoexcited state dynamics of large linear conjugated systems.

In this paper we also explore in more detail the excited state dynamics as a function of the broken-symmetry perturbation that connects the diabatic states of opposite particle-hole symmetry. We show that for a small perturbation, the system undergoes a transition from the initial adiabatic state, S_1 , to S_2 , while remaining in the same diabatic state, $1^1B_u^+$. In contrast, for larger perturbations, the system evolves adiabatically on the S_1 surface, changing character from the excitonic $1^1B_u^+$ state to the singlet triplet-pair $2^1A_g^-$ state. In all cases the S_1 and S_2 energies exhibit an avoided crossing, and the dynamics can be approximately modeled as a two-level system.

2 Model Hamiltonian and eigenstates

2.1 UV-Peierls Hamiltonian

The PPP Hamiltonian, routinely utilized with static DMRG for modelling electronic properties of conjugated polymers, contains long range Coulomb interactions and therefore is not readily suitable for dynamical simulations using the adaptive time-dependent DMRG (tDMRG) algorithm. In a tDMRG setting, the electronic degrees of freedom are conveniently described by the extended Hubbard (UV) Hamiltonian, defined by

$$\hat{H}_{\text{UV}} = -2\beta \sum_{n=1}^{N-1} \hat{T}_n + U \sum_{n=1}^N \left(\hat{N}_{n\uparrow} - \frac{1}{2} \right) \left(\hat{N}_{n\downarrow} - \frac{1}{2} \right) + \frac{1}{2} \sum_{n=1}^{N-1} V (\hat{N}_n - 1) (\hat{N}_{n+1} - 1), \quad (1)$$

where n labels the n^{th} C-atom, N is the number of conjugated C-atoms and $N/2$ is the number of double-bonds. $\hat{T}_n = \frac{1}{2} \sum_{\sigma} \left(\hat{c}_{n,\sigma}^{\dagger} \hat{c}_{n+1,\sigma} + \hat{c}_{n+1,\sigma}^{\dagger} \hat{c}_{n,\sigma} \right)$ is the bond order operator, $\hat{c}_{n,\sigma}^{\dagger} (\hat{c}_{n,\sigma})$ creates (destroys) an electron with spin σ in the p_z orbital of the n^{th} C-atom, and \hat{N}_n is the number operator. U and V correspond to Coulomb parameters which describe interactions of two electrons in the same orbital and nearest neighbors respectively, and β represents the electron hopping integral between neighboring C-atoms. The UV-Peierls Hamiltonian is invariant to a particle-hole transformation. For idealized carotenoid structures with C_2 symmetry, its eigenstates will have definite C_2 and particle-hole symmetries.²⁷

With the inclusion of nuclear degrees of freedom, the UV-Peierls Hamiltonian is defined by

$$\hat{H}_{\text{UVP}} = \hat{H}_{\text{UV}} + 2\alpha \sum_{n=1}^{N-1} (u_{n+1} - u_n) \hat{T}_n + \frac{K}{2} \sum_{n=1}^{N-1} (u_{n+1} - u_n)^2, \quad (2)$$

where α is the electron-nuclear parameter, K is the nuclear spring constant, and u_n is the displacement of the n^{th} carbon atom from its undistorted geometry. Electron hopping integrals relate to nuclear geometries via $\beta_n = \beta - \alpha(u_{n+1} - u_n)$.

2.2 Broken symmetry

In order to facilitate internal conversion from the photoexcited $1^1B_u^+$ state to the triplet-pair states (which are of negative particle-hole character), an interaction term which breaks the particle-hole symmetry is introduced.¹ The symmetry breaking term is defined by

$$\hat{H}_\epsilon = \sum_{n=1}^N \epsilon_n (\hat{N}_n - 1), \quad (3)$$

where ϵ_n is the on-site potential energy parameter on the n^{th} C-atom. The inclusion of H_ϵ is justified as carotenoids with both electron donating and withdrawing substituent groups (e.g., neurosporene shown in Figure 1), which act as electron donors and acceptors to the π -system, are known to undergo singlet fission.⁵⁷

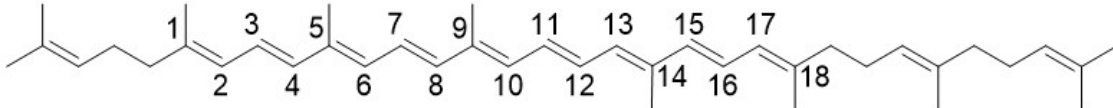


Figure 1: Neurosporene, a naturally occurring carotenoid with 18 conjugated carbon atoms.

Since we are only interested in the singlet excitations, we project out the high spin contributions to the Hilbert space by supplementing the Hamiltonian with

$$\hat{H}_\lambda = \lambda \hat{S}^2, \quad (4)$$

where \hat{S} is the total spin operator, and $\lambda > 0$.

We now define the full Born-Oppenheimer Hamiltonian as

$$\hat{H} = \hat{H}_{\text{UVP}} + \hat{H}_\lambda + \hat{H}_\epsilon. \quad (5)$$

¹We follow the particle-hole sign convention of ref 56, which is commonly used by the experimental community but is the opposite definition to refs 25 and 27.

Eigenstates of \hat{H} are labelled adiabatic (singlet) eigenstates, and are defined by

$$\hat{H} |S_i\rangle = E_i |S_i\rangle. \quad (6)$$

We define a diabatic (singlet) basis spanned by the eigenstates of $(\hat{H}_{\text{UVP}} + \hat{H}_\lambda)$ as

$$(\hat{H}_{\text{UVP}} + \hat{H}_\lambda) |\phi_j\rangle = E_{\phi_j} |\phi_j\rangle. \quad (7)$$

The diabatic eigenstates have definite C_2 and particle-hole symmetries.

We calculate the probability that the system described by $\Psi(t)$ occupies the adiabatic state S_i by

$$P(\Psi(t); S_i) = |\langle S_i | \Psi(t) \rangle|^2 \quad (8)$$

and the probability that it occupies the diabatic state ϕ_j by

$$P(\Psi(t); \phi_j) = |\langle \phi_j | \Psi(t) \rangle|^2. \quad (9)$$

Finally, the probability that the adiabatic S_i occupies the diabatic ϕ_j is

$$P(S_i; \phi_j) = |\langle \phi_j | S_i \rangle|^2. \quad (10)$$

For our simulations, we first determine the ground state of the system using the static DMRG method by solving eq (2) for fixed nuclear displacements, $\{u_n\}$. Starting from the undimerised geometry ($u_n = 0, \forall n$), ground and excited state energies and geometries are found by iterative application of eq (36) with the force per atom n , $f_n = 0$.²⁵ The initial system, $\Psi(t = 0)$, is taken to be the adiabatic singlet state S_i with the largest projection onto the $1^1B_u^+$ diabatic, determined via eq (10). This corresponds to a dipole-allowed vertical excitation from the ground state, S_0 . The choice to define the initial system this way, instead of as $\hat{\mu}S_0$, is based on the observation that the Ehrenfest approximation (discussed in section

4.1) is most accurate for systems evolving on a single adiabatic potential energy surface.

Diabatic eigenstates of $\hat{H} = (\hat{H}_{\text{UVP}} + \hat{H}_\lambda)$ with a positive particle-hole symmetry are termed ‘ionic’, as the expectation value of the ionicity operator, $\hat{I} = \sum_n (\hat{N}_n - 1)^2$, is larger for these states than for eigenstates with a negative particle-hole symmetry, termed ‘covalent’. We use this property of a larger ionicity for ionic states to distinguish them from covalent states during the dynamical simulation.

2.3 Parametrizations

2.3.1 UVP Model parametrization

The UV Hamiltonian does not contain the long-range Coulomb interactions of the PPP Hamiltonian, and therefore requires a parametrization of the U and V Coulomb parameters to replicate the PPP model predictions. While retaining the Chandross-Mazumdar parametrization of $\beta = 2.4$ eV,⁴⁹ $K = 46$ eV Å⁻² and $\alpha = 4.593$ eV Å⁻¹ from Barford and co-workers,²⁵ in our earlier work⁵⁴ we parametrized the UV model for internal conversion from $1^1B_u^+$ to $1^1B_u^-$ to reproduce the predictions of ref 56.

In our companion paper,⁵⁵ we model internal conversion from the $1^1B_u^+$ state to both the $1^1B_u^-$ and $2^1A_g^-$ states. For the latter, we require a parametrization where $E_{1^1B_u^+}(\text{vertical}) < E_{2^1A_g^-}(\text{vertical})$. For a given U , increasing V decreases $(E_{1^1B_u^+} - E_{2^1A_g^-})$. Keeping all other parameters the same (i.e., $U = 7.25$ eV and $\beta = 2.4$ eV), we find $V = 3.25$ eV such that $E_{1^1B_u^+}(\text{vertical}) - E_{2^1A_g^-}(\text{vertical})$ replicates the lowest-lying carotenoid dark and bright state vertical excitation energies reported in Table 2 of ref 32. The diabatic vertical and relaxed energies for the UV-Peierls model with these parameters are illustrated in Figure 2. (The corresponding figures where $E_{1^1B_u^+}(\text{vertical}) > E_{2^1A_g^-}(\text{vertical})$ for $U = 7.25$ eV, $\beta = 2.4$ eV, and $V = 2.75$ eV are shown in ref 54). For all carotenoid chain lengths under consideration, $1^1B_u^+$ vertical energies lie below $2^1A_g^-$ vertical energies, while $1^1B_u^+$ relaxed energies are above $2^1A_g^-$ relaxed energies, indicating the possibility of internal conversion from the $1^1B_u^+$ to the $2^1A_g^-$ states via a diabatic energy level crossing. Internal conversion to the $2^1A_g^-$ state could

potentially lead to endothermic intramolecular singlet fission, as the relaxed energy of the $2^1A_g^-$ state is lower than the energy of two triplets on the same chain. However, as shown in ref 55, exothermic intermolecular singlet fission is possible provided that the carotenoids are twisted in their ground state.

2.3.2 Parametrizing \hat{H}_ϵ

The symmetry breaking term (eq (3)) alters the on-site potential energies, and therefore changes the Mulliken charge densities of the π -system from unity. As outlined below, we use the ground state Mulliken charge densities of the π -system to parametrize H_ϵ for neosporene, whose structural formula is illustrated in Figure 1. The optimum Mulliken charge densities are calculated using the ORCA program package.^{58,59} Geometry optimizations are performed using density functional theory (DFT) with a B3LYP functional⁶⁰ and a def2-TZVP basis set,^{61,62} followed by calculations of electron densities. To enforce charge neutrality in our model, the mean shifted Mulliken charge densities are used as target densities in an optimization algorithm to determine \hat{H}_ϵ .

Allowing unconstrained optimization of \hat{H}_ϵ leads to unphysical on-site potential energies and significant changes in the character of excited states. In order to avoid large perturbations, we use projected gradient descent algorithm to search for $\epsilon = (\epsilon_1, \epsilon_2 \dots \epsilon_N)$ such that $|\epsilon_i| < \epsilon_{\max}, \forall i \in \{1, 2, \dots, N\}$.⁶³ For a given ϵ , $\mathbf{d} = (d_1, d_2, \dots, d_N)$ where $d_i = \langle \Psi | \hat{N}_i - 1 | \Psi \rangle$ can be found via the static DMRG algorithm. We define the minimization function as $E(\epsilon) = \|\mathbf{d}_{\text{opt}} - \mathbf{d}(\epsilon)\|$ where \mathbf{d}_{opt} is the target density vector found via DFT. The algorithm is as follows:

1. Choose initial ϵ_0 within the constraints
2. Loop until the convergence condition is met:
 - (a) Find the descent direction $-\nabla E(\epsilon_k)$
 - (b) Find $\bar{\epsilon}_{k+1} = \epsilon_k - \nabla E(\epsilon_k)$

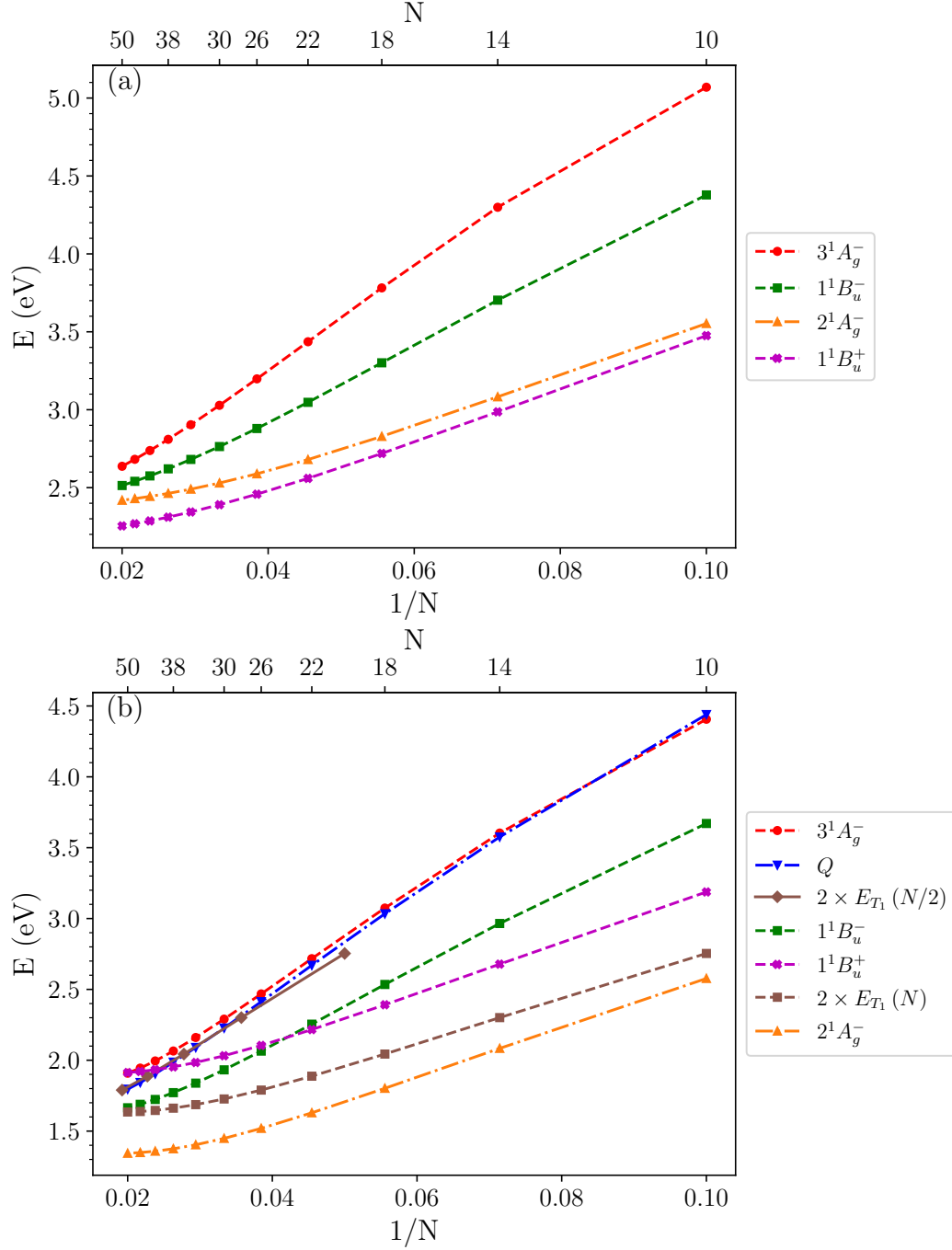


Figure 2: Vertical (a) and relaxed (b) singlet excitation energies of the UV-Peierls model with $U = 7.25$ eV and $V = 3.25$ eV, found by solving eq (2). N is the number of conjugated carbon atoms of the system. The vertical energy gaps of ~ 0.1 eV between $1^1B_u^+$ (magenta) and $2^1A_g^-$ (orange) for $18 \leq N \leq 26$ agree with the corresponding excitation energies reported in ref. ³²

(c) Projection: Find $\epsilon_{k+1} = (\epsilon_1^{k+1}, \epsilon_2^{k+1} \dots \epsilon_N^{k+1})$ such that $\forall i \in \{1, 2, \dots, N\}$,

$$\epsilon_i^{k+1} = \begin{cases} \bar{\epsilon}_i^{k+1} & , |\bar{\epsilon}_i^{k+1}| \leq \epsilon_{\max} \\ \epsilon_{\max} & , \bar{\epsilon}_i^{k+1} > \epsilon_{\max} \\ -\epsilon_{\max} & , \bar{\epsilon}_i^{k+1} < -\epsilon_{\max} \end{cases} \quad (11)$$

3. Convergence is evaluated via the coefficient of variation $r^2(\epsilon)$ defined as:

$$r^2(\epsilon) = 1 - \frac{[E(\epsilon)]^2}{\|\mathbf{d}_{\text{opt}}\|^2} \quad (12)$$

Table 1: The π -electron Mulliken charges from the *ab-initio* DFT calculation, parameters for the symmetry-breaking term, \hat{H}_ϵ , and the expectation values of number densities calculated from the parametrized \hat{H}_ϵ . In order to maintain π -electron charge neutrality, each *ab-initio* charge was increased by $0.05q$. The chemical formula of neurosporene is shown in figure 1.

Carbon site, n	Mulliken charges (q)	ϵ_n (eV)	$\langle \hat{N}_n - 1 \rangle$
1	0.14	-1.00	0.17
2	-0.18	0.56	-0.14
3	-0.05	1.00	0.06
4	-0.18	0.82	-0.10
5	0.15	-1.00	0.15
6	-0.14	0.02	-0.10
7	-0.07	1.00	0.03
8	-0.16	0.84	-0.09
9	0.13	-1.00	0.12
10	-0.09	-0.01	-0.07
11	-0.11	1.00	-0.04
12	-0.10	1.00	-0.03
13	-0.11	0.09	-0.09
14	0.14	-1.00	0.13
15	-0.18	0.92	-0.10
16	-0.05	1.00	0.06
17	-0.19	0.61	-0.14
18	0.14	-1.00	0.17

We perform the optimization for $\epsilon_{\max} = 1.0$ eV. For the simulations described in ref 55, ϵ_{\max} is constrained to an upper bound of 1.0 eV to prevent the formation of an unphysical

potential energy gradients across the conjugated carbon atoms which causes an unphysical mixing of the ionic and covalent states. (However, the effect of an arbitrary symmetry-breaking potential is described in section 7.2 of this paper.) The optimized \hat{H}_ϵ found for neurosporene with $V = 3.25$ eV and $r^2(\epsilon) = 0.92$ is shown in Table 1.

3 Density Matrix Renormalization Group (DMRG)

From now on in this paper we define a ‘site’ as a p_z orbital of a C-atom. The single-site basis for the UVP model defined in eq (2), i.e., $\{ \text{---}, \text{---} \vdash, \text{---} \vdash, \text{---} \vdash \}$, has a dimensionality of 4. Therefore, exactly solving the time-dependent Schrödinger equation for $N = 18$, the relevant carotenoid chain length, would require solving a $S_z = 0$ Hilbert space of size $\approx 2.4 \times 10^9$. This is not feasible in realistic time scales. DMRG methods are based on the premise that by an efficient truncation of the exact Hilbert space to retain only the important many-particle states, the most important features of the system can be preserved at a significantly lower computational cost. We begin this section by describing the static DMRG algorithm and then show how the method can easily be extended to the adaptive time-dependent DMRG (tDMRG) algorithm.

3.1 Static DMRG algorithm

The infinite DMRG algorithm was introduced in 1992 to accurately calculate ground states of one-dimensional quantum systems.²¹ Suppose that a system of length $(k - 1)$ described by a Hilbert space of size M_l is spanned by the basis states $\{|l_{k-1}\rangle\}$. Consider the process of the linear growth of this system block by adding a single site at index k (see Figure 3). The single site is fully described by the d -dimensional basis $\{|\alpha_k\rangle\}$. An augmented system block of length k is constructed in the product Hilbert space spanned by $\{|l_{k-1}\rangle \otimes |\alpha_k\rangle\}$, with dimensions $N_S = M_l \times d$. An analogous augmented environment is constructed in the product Hilbert space spanned by $\{|\alpha_{k+1}\rangle \otimes |r_{k-1}\rangle\}$, with dimensions $N_E = M_r \times d$. A

superblock of length $2k$ is now formed in the product Hilbert space spanned by $\{|l_{k-1}\rangle \otimes |\alpha_k\rangle \otimes |\alpha_{k+1}\rangle \otimes |r_{k-1}\rangle\}$. The ground state,

$$|\Psi\rangle = \sum_{l_{k-1}=1}^{M_l} \sum_{\alpha_k=1}^d \sum_{\alpha_{k+1}=1}^d \sum_{r_{k-1}=1}^{M_r} \Psi_{l_{k-1}, \alpha_k, \alpha_{k+1}, r_{k-1}} |l_{k-1}\rangle |\alpha_k\rangle |\alpha_{k+1}\rangle |r_{k-1}\rangle, \quad (13)$$

is obtained by a sparse-matrix diagonalization (e.g., conjugate gradient or Davidson) of the Hamiltonian in the superblock basis.

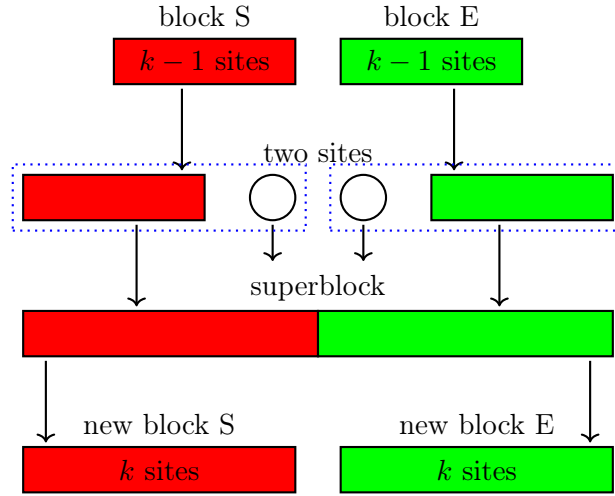


Figure 3: Schematic diagram illustrating one iteration of the infinite DMRG algorithm.⁶⁴

Defining the augmented system block state $|i\rangle \in \{|l_{k-1}\rangle \otimes |\alpha_k\rangle\}$, and the augmented environment block state $|j\rangle \in \{|\alpha_{k+1}\rangle \otimes |r_{k-1}\rangle\}$, the ground state may also be expressed as,

$$|\Psi\rangle = \sum_{i=1}^{N_S} \sum_{j=1}^{N_E} \Psi_{i,j} |i\rangle |j\rangle. \quad (14)$$

Now a truncation procedure must be introduced to describe the system block of size k using a basis of dimension $M_S < N_S$. Suppose that the ground state of the system can be expressed by the approximate state $|\tilde{\Psi}\rangle$ in this truncated Hilbert space,

$$|\tilde{\Psi}\rangle = \sum_{p=1}^{M_S} \sum_{j=1}^{N_E} \tilde{\Psi}_{p,j} |p\rangle |j\rangle. \quad (15)$$

Finding the optimum $|\tilde{\Psi}\rangle$ is achieved by the minimization of the quadratic norm S_2 ,

$$S_2 = \|\Psi\rangle - |\tilde{\Psi}\rangle\|^2. \quad (16)$$

From eq (14), we see that Ψ can be recast into a rectangular matrix of dimension $N_S \times N_E$, which can then be decomposed using singular value decomposition as

$$\Psi = UDV^\dagger, \quad (17)$$

where U is a unitary matrix of dimension $N_S \times N_E$, V is a unitary matrix of dimension $N_E \times N_E$, and D is a diagonal matrix of dimension $N_E \times N_E$ with elements $\{\lambda_\beta\}$. This transformation implies that $|\Psi\rangle$ can be expressed as a Schmidt decomposition,

$$|\Psi\rangle = \sum_{\beta=1}^r \lambda_\beta |\beta_S\rangle |\beta_E\rangle, \quad (18)$$

where $|\beta_S\rangle = \sum_i U_{i,\beta} |i\rangle$, $|\beta_E\rangle = \sum_j V_{\beta,j}^* |j\rangle$, and $r = \min(N_S, N_E)$.²² It follows that in the Schmidt basis, the reduced density operator $\hat{\rho}_S = \text{tr}_E |\Psi\rangle \langle \Psi|$ can be written as

$$\hat{\rho}_S = \sum_{\beta=1}^{N_S} \lambda_\beta^2 |\beta_S\rangle \langle \beta_S|, \quad (19)$$

where $|\beta_S\rangle$ and $\lambda_\beta^2 = \omega_\beta$ are the eigenstates and eigenvalues, respectively, of the reduced density operator.

The quadratic norm S_2 is given by

$$S_2 = \sum_{\beta=1}^r \omega_\beta - \sum_{\beta=1}^{M_S} \omega_\beta = \sum_{\beta=M_S+1}^r \omega_\beta. \quad (20)$$

S_2 is therefore minimized by retaining the M_S eigenstates of $\hat{\rho}_S$ with the largest eigenvalues.

Once the truncated basis for the new system block of length k , $\{|l_k\rangle\}$ is known, all

operators, including the Hamiltonian, are rotated to the new Hilbert space via a similarity transformation. Suppose $\hat{O} = \sum_{n=1}^k \hat{O}_n$ is a generic operator. Then \hat{O}_k is given by

$$\langle l_k | \hat{O}_k | \tilde{l}_k \rangle = \sum_{l_{k-1}=1}^{M_l} \sum_{\alpha_k=1}^d \sum_{\tilde{\alpha}_k=1}^d \langle l_k | l_{k-1} \rangle \otimes |\alpha_k\rangle \langle \alpha_k | \hat{O}_k | \tilde{\alpha}_k \rangle \langle l_{k-1} | \otimes \langle \tilde{\alpha}_k | \tilde{l}_k \rangle. \quad (21)$$

\hat{O}_n where $n < k$ is transformed to the truncated Hilbert space by

$$\langle l_k | \hat{O}_n | \tilde{l}_k \rangle = \sum_{l_{k-1}=1}^{M_l} \sum_{\tilde{l}_{k-1}=1}^{M_l} \sum_{\alpha_k=1}^d \langle l_k | l_{k-1} \rangle \otimes |\alpha_k\rangle \langle l_{k-1} | \hat{O}_n | \tilde{l}_{k-1} \rangle \langle \tilde{l}_{k-1} | \otimes \langle \alpha_k | \tilde{l}_k \rangle. \quad (22)$$

The total Hamiltonian is not known during the intermediate steps of the infinite DMRG algorithm, and this leads to errors, especially in systems with strong physical effects from impurities or randomness in the Hamiltonian.⁶⁴ These finite size effects can be resolved by performing finite ‘sweeps’ after the infinite DMRG. Once the desired system size N is reached, the steps of infinite DMRG is continued, but with one block (system) growing at the expense of the other (environment). The superblock size remains fixed at N , and truncation of the basis is only performed for the growing block. Determination of the superblock ground state is efficiently implemented using the White’s wavefunction mapping algorithm,⁶⁵ where the ground state found during the previous step of the sweep is rotated into the new Hilbert space to be used as a trial state for the diagonalization procedure. This procedure is continued until the shrinking block only contains a single site, and then the direction of the sweep is reversed. Several finite DMRG sweeps are performed until the desired convergence is reached. The finite DMRG algorithm is illustrated in Figure 4.

By exploiting the sparsity of the block symmetry operators (e.g., the particle-hole and spin-flip symmetries), excited states are conveniently determined by constructing symmetry-adapted states.⁵³ Within a symmetry sector higher-lying states are then determined via a Gram-Schmidt projection. In order to accurately describe these excited states, it is necessary to retain the basis states that optimally represent them in the truncated Hilbert space. This

is achieved by including them in the reduced density matrix, i.e.,

$$\hat{\rho}_S = \text{tr}_E \sum_i \kappa_i |\Psi_i\rangle \langle \Psi_i|, \quad (23)$$

where the summation includes all the targeted states. κ_i is usually chosen to be the same for all states such that $\sum_i \kappa_i = 1$.

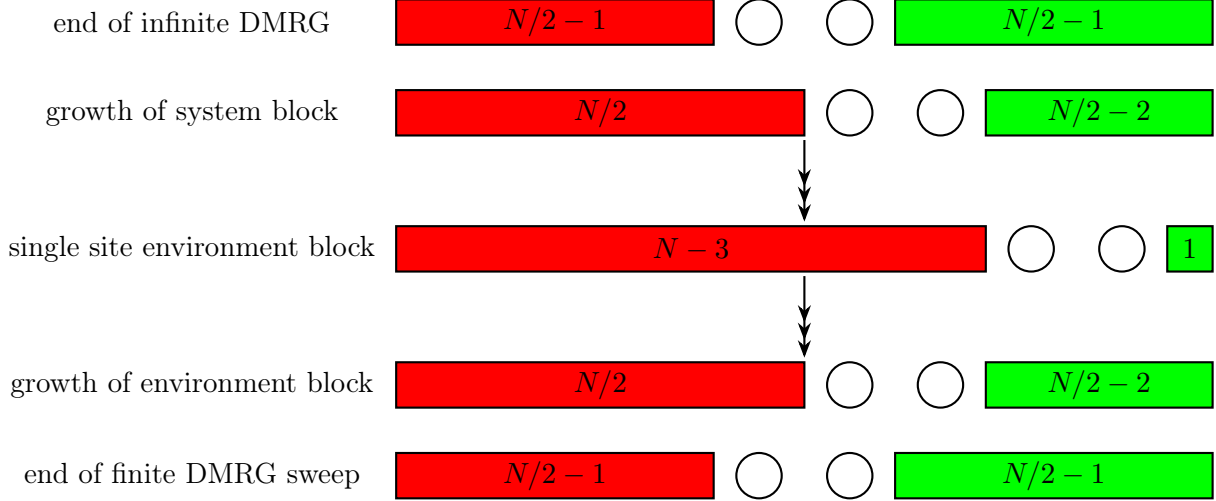


Figure 4: Schematic diagram for the finite DMRG algorithm illustrating a single finite lattice sweep.⁶⁴ The number of sites in each block is shown as text. An open circle represents a single site block.

3.2 Adaptive Time-dependent DMRG (tDMRG)

The dynamics of the evolving system under the Hamiltonian \hat{H} is fully determined by solving the time-dependent Schrödinger equation

$$i\hbar \frac{\partial}{\partial t} |\Psi(t)\rangle = \hat{H}(t) |\Psi(t)\rangle. \quad (24)$$

In the limit that $\delta t \rightarrow 0$, eq (24) has the formal solution

$$|\Psi(t + \delta t)\rangle = \exp \left(-i\hat{H}(t)\delta t/\hbar \right) |\Psi(t)\rangle. \quad (25)$$

The adaptive time-dependent density matrix renormalization group method, developed in 2004, generalised the DMRG algorithm to study time dependent phenomena.^{34,35} In this formalism, the evolving state $|\Psi(t)\rangle$ is determined in a truncated Hilbert space such that the loss of information about the system is minimized. The algorithm is efficiently implemented for Hamiltonians containing only on-site and nearest neighbor interactions. Such a Hamiltonian can be written as a sum of bond Hamiltonians,

$$\hat{H} = \hat{H}_{1,2} + \hat{H}_{2,3} + \hat{H}_{3,4} + \cdots \hat{H}_{n,n+1} + \cdots + \hat{H}_{N-1,N}, \quad (26)$$

where $\hat{H}_{n,n+1} = \frac{1}{2} \left(\hat{H}_n^{\text{intra}} + \hat{H}_{n+1}^{\text{intra}} \right) + \hat{H}_{n,n+1}^{\text{inter}}$ acts on the n^{th} bond. Since neighboring bond Hamiltonians do not commute, a Suzuki-Trotter decomposition is invoked for the propagator, i.e.,

$$e^{-i\hat{H}\delta t/\hbar} \approx e^{-i\hat{H}_{1,2}\delta t/2\hbar} e^{-i\hat{H}_{2,3}\delta t/2\hbar} \cdots e^{-i\hat{H}_{N-1,N}\delta t/2\hbar} e^{-i\hat{H}_{N-1,N}\delta t/2\hbar} \cdots e^{-i\hat{H}_{2,3}\delta t/2\hbar} e^{-i\hat{H}_{1,2}\delta t/2\hbar} + O(\delta t^3) \quad (27)$$

The link time evolution operator, $\hat{U}_n = e^{-i\hat{H}_{n,n+1}\delta t/2\hbar}$, is exactly applied on $|\Psi(t)\rangle$ at DMRG step $(n-1)$.³⁵ At this step the DMRG state is

$$|\Psi\rangle = \sum_{l,\alpha_n,\alpha_{n+1},r} \Psi_{l,\alpha_n,\alpha_{n+1},r} |l_{n-1}\rangle |\alpha_n\rangle |\alpha_{n+1}\rangle |r_{N-(n+1)}\rangle. \quad (28)$$

The states $|l_{n-1}\rangle$ and $|r_{N-(n+1)}\rangle$ are eigenvectors of the reduced density matrices corresponding to the system and environment DMRG blocks at step n . The states $|\alpha_n\rangle$ and $|\alpha_{n+1}\rangle$ are the exact basis states for sites n and $n+1$.

To find $|\Phi\rangle = \hat{U}_n |\Psi\rangle$, the 2-site augmented block state $|m\rangle = |\alpha_n\rangle |\alpha_{n+1}\rangle$ is transformed to the basis spanned by the eigenstates of $\hat{H}_{n,n+1}$, i.e., $\hat{H}_{n,n+1} |m\rangle = \epsilon_m |m\rangle$, where

$$|m\rangle = \sum_{m'} \phi_{m',m} |m'\rangle. \quad (29)$$

With this transformation, $|\Phi\rangle = \hat{U}_n |\Psi\rangle$ can be written as,

$$|\Phi\rangle = \sum_{l,m'',r} \sum_{m,m'} e^{-i\epsilon_{m'}\delta t/2\hbar} \phi_{m,m'} \phi_{m'',m'} \Psi_{l,m,r} |l\rangle |m''\rangle |r\rangle. \quad (30)$$

The algorithm now proceeds in precisely the same way as for the static finite lattice DMRG method, namely $|\Phi\rangle$ is truncated via a singular value decomposition and is then transformed to the basis for the next DMRG step via White's wavefunction mapping technique.⁶⁵ Figure 5 illustrates the key steps of the adaptive tDMRG algorithm.

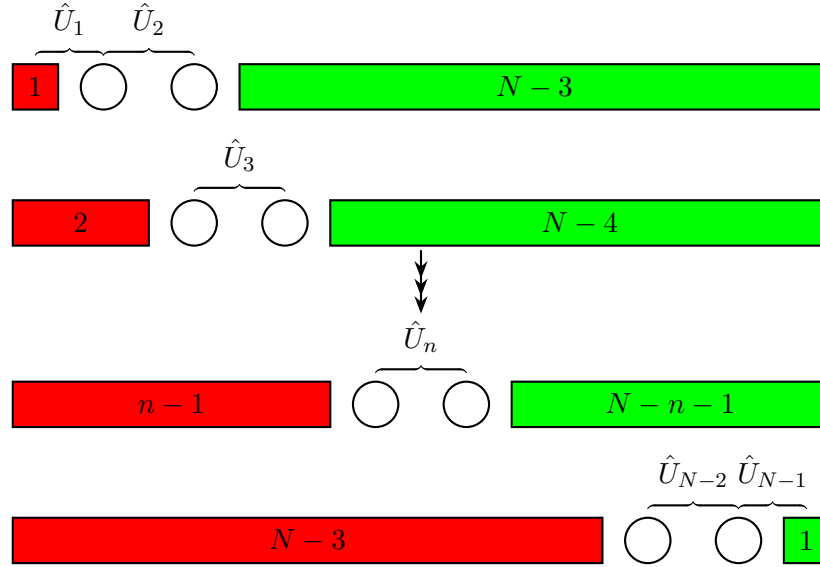


Figure 5: Schematic diagram for a single sweep of the adaptive tDMRG algorithm, illustrating the application of the time evolution operator for a time of $\Delta t/2$. The number of sites in each block is shown as text. An open circle represents a single site block. $\hat{U}_n = e^{-i\hat{H}_{n,n+1}\delta t/2\hbar}$.

Readers are referred to refs 64, 66 for a comprehensive review of the DMRG, refs 67–69 for recent reviews of applications of DMRG in quantum chemistry, and ref 70 for a review of time-dependent density matrix renormalization group methods.

3.3 DMRG accuracy

As discussed in section 3.1, the DMRG algorithm finds the optimum $|\tilde{\Psi}\rangle$ by minimizing the quadratic norm S_2 (see eq (20)). The truncation error, ϵ , associated with the DMRG

algorithm can therefore be defined as the sum of the eigenvalues of $\hat{\rho}_S$ disgarded during the DMRG truncation, i.e.,

$$\epsilon = \min(S_2) = 1 - \sum_{\beta=1}^{M_S} \omega_{\beta}, \quad (31)$$

and $\sum_{\beta=1}^r \omega_{\beta} = 1$. The reason for the remarkable success of DMRG in explaining the properties of one dimensional quantum systems is understood by the realization that the DMRG truncation error is closely related to the amount of information that is required to accurately represent a quantum system.^{71,72} This amount of information is dependent on the entanglement of the system, and is quantified via the von Neumann entanglement entropy,

$$S = - \sum_{\beta=1}^r \lambda_{\beta}^2 \log \lambda_{\beta}^2 = - \text{Tr}_S(\hat{\rho}_S \log \hat{\rho}_S). \quad (32)$$

To illustrate this quantity, first consider a fully unentangled system. This state is described by a product state given by

$$|\Psi\rangle = \left(\sum_{i=1}^{N_S} \Psi_i |i\rangle \right) \otimes \left(\sum_{j=1}^{N_E} \Psi_j |j\rangle \right). \quad (33)$$

It follows that for this state, $\hat{\rho}_S = |\Phi_S\rangle \langle \Phi_S|$ where $|\Phi_S\rangle = \sum_{i=1}^{N_S} \Psi_i |i\rangle$, and thus $S = 0$. Therefore, the unentangled state has the minimum von Neumann entropy. To demonstrate the maximally entangled state, consider a two spin system described by

$$|\Psi\rangle = \frac{1}{\sqrt{2}} (|\uparrow_S\rangle |\downarrow_E\rangle + |\downarrow_S\rangle |\uparrow_E\rangle). \quad (34)$$

For this state, $\hat{\rho}_S = \frac{1}{2} (|\uparrow_S\rangle \langle \uparrow_S| + |\downarrow_S\rangle \langle \downarrow_S|)$ and $S = \log 2$. In general, for the maximally entangled state, if the rank of the Schmidt decomposition is r , then $\omega_{\beta} = \lambda_{\beta}^2 = 1/r$, and $S = \log r$.

Recall from eq (18) that a general state $|\Psi\rangle$ can be written using a Schmidt basis, where the Schmidt coefficients λ_{β} are related to the eigenvalues of $\hat{\rho}_S$ by $\omega_{\beta} = \lambda_{\beta}^2$. Thus, if the

eigenvalues $\{\omega_\beta\}$ decay rapidly, only a small error is introduced by retaining only a relatively small number of eigenstates.

The growth of entanglement with systems size is related to the ‘area law’ which explains why DMRG works so well for one-dimensional systems, but fails in higher dimensions.⁷³ The area law states that the entanglement entropy of the ground state of a gapped, partitioned system is proportional to the size of the partition between the systems. For one-dimensional systems, the surface between two systems is a point, and as this does not change with system size the entanglement entropy is a constant with system size.⁷⁴ This further implies that the truncation error remains essentially constant for a fixed system basis size as a function of system size. DMRG is thus highly suitable for the study of the electronic states of insulating polyene systems.

4 Nuclear degrees of freedom

4.1 Ehrenfest dynamics

While the electronic wavefunction determined by solving the TDSE is achieved using adaptive tDMRG, the dynamics of the nuclei are determined via the Ehrenfest equations of motion. The Ehrenfest method assumes that the nuclei evolve on a single effective potential energy surface corresponding to an average of the electronic states contributing to the electronic wavefunction. As a result, despite its mean-field nature, the Ehrenfest method is able to describe transitions between different electronic states.⁷⁵

The nuclear degrees of freedom, defined by eq (2), are treated classically via the Hellmann-Feynman theorem. The force on atom n , f_n is

$$f_n = -\frac{\delta\langle\Psi|\hat{H}|\Psi\rangle}{\delta u_n} = -\left\langle\frac{\delta\hat{H}}{\delta u_n}\right\rangle. \quad (35)$$

This leads to

$$f_n = 2\alpha \left(\langle \hat{T}_n \rangle - \langle \hat{T}_{n-1} \rangle \right) - K (2u_n - u_{n+1} - u_{n-1}). \quad (36)$$

The nuclei obey Newton's equations of motion

$$\frac{du_n(t)}{dt} = \frac{p_n(t)}{m} \quad (37)$$

and

$$\frac{dp_n(t)}{dt} = f_n(t) - \gamma p_n(t), \quad (38)$$

where p_n and m are the nuclear momentum and mass, respectively. A phenomenological linear damping term γp_n is introduced to cause relaxation of the nuclei. The equations of motion are propagated using the damped Velocity Verlet scheme derived in appendix 5.A of reference 76, i.e.,

$$u_n(t + \Delta t) = u_n(t) + \frac{p_n(t)}{m} \Delta t + \frac{1}{2} \frac{[f_n(t) - \gamma p_n(t)]}{m} \Delta t^2 \quad (39)$$

$$p_n(t + \Delta t) = \frac{1}{1 + \Delta t \gamma / 2} \left[p_n(t) [1 - \Delta t \gamma / 2] + \frac{\Delta t}{2} ([f_n(t + \Delta t) + f_n(t)]) \right]. \quad (40)$$

4.2 Validity of Ehrenfest dynamics

Molecular dynamics is routinely utilized to simulate numerical dynamics of a diverse range of chemical processes, including gas phase molecular collisions,⁷⁷ reactions in liquids,⁷⁸ biomolecular dynamics.⁷⁹ At the heart of the molecular dynamics method is the adiabatic or the Born-Oppenheimer approximation, the assumption that electronic degrees of freedom instantaneously adjust to the nuclear motion such that the electrons move on a single adiabatic surface. Dynamical processes involving electronic transitions violate the Born-Oppenheimer approximation, and as a consequence molecular dynamics is inadequate for the description of dynamical processes involving electronic transitions, and nonadiabatic methods are required.

Ehrenfest dynamics is a non-adiabatic method where the 'slow' nuclear degrees of freedom

evolve on an effective potential energy surface defined by the weighted average of contributing adiabatic surfaces.⁷⁵ The Ehrenfest method allows for feedback between the nuclear and electronic degrees of freedom in both directions, and therefore is a self-consistent method. It is routinely used to model nonadiabatic dynamics.^{80–84} While Ehrenfest dynamics produce accurate results if the coupled adiabatic states are similar in character, due to its mean-field nature it fails to properly describe dynamics if the wavepacket bifurcates onto adiabatic surfaces with very different character.⁷⁵

Tully’s surface hopping technique was developed to overcome the erroneous mean-field approximation of the Ehrenfest method.⁸⁵ The nuclear degrees of freedom moves on a single potential energy surface until a region of large nonadiabatic coupling is encountered, at which the trajectory splits stochastically. Another approach to improve on the Ehrenfest method is to incorporate quantum effects to the nuclear degrees of freedom. Mannouch and Barford developed the TEBD-Ehrenfest method for the dynamical simulations of Frenkel-Holstein model.^{43,44,86} Nuclear motion is described by a mean-field displacement subjected to Ehrenfest dynamics, with quantum fluctuations around the mean-field value. In future work, the TEBD-Ehrenfest algorithm described in ref. 44 will be generalized for Debye phonons and its performance will be compared with dynamical simulations based on Ehrenfest equations of motion of refs 54 and 55.

5 Lanczos-DMRG

Transient (time-resolved) absorption experiments are among the most routinely utilized experimental techniques in the field of carotenoid photophysics.⁸⁷ A typical transient absorption measurement involves photoperturbation of the dynamical system at time t and measurement of the effect of the perturbation at time $t + \tau$. This corresponds to the dynamical correlation function $\tilde{G}_\mu(t, \tau)$ defined as

$$\tilde{G}_\mu(t, \tau) = \langle \Psi(t) | \hat{\mu}(t + \tau) \hat{\mu}(t) | \Psi(t) \rangle, \quad (41)$$

where $\hat{\mu}(t)$ is the Heisenberg representation of the dipole moment operator $\hat{\mu}$. Via a Fourier transform of ω with respect to τ , we obtain the dynamical correlation function in the frequency domain as⁸⁸

$$G_\mu(t, \omega + i\hbar\eta) = -\frac{1}{\pi} \left\langle \Psi(t) \left| \hat{\mu} \frac{1}{E_\Psi + \omega + i\hbar\eta - \hat{H}} \hat{\mu} \right| \Psi(t) \right\rangle, \quad (42)$$

where E_Ψ is the energy of $|\Psi(t)\rangle$, and η is a small positive real number used to shift the poles of $G_\mu(t, \omega)$ into the complex plane. The imaginary part of $G_\mu(t, \omega + i\hbar\eta)$ is given by

$$I_\mu(t, \omega + i\hbar\eta) = \frac{1}{\pi} \left\langle \Psi(t) \left| \hat{\mu} \frac{\eta}{(E_\Psi + \omega - \hat{H})^2 + \hbar^2\eta^2} \hat{\mu} \right| \Psi(t) \right\rangle. \quad (43)$$

If a complete set of eigenstates $\{|n\rangle\}$ of \hat{H} , with eigenvalues $\{E_n\}$ is known, using $\hat{1} = \sum_n |n\rangle \langle n|$, we can write

$$I_\mu(t, \omega + i\hbar\eta) = \frac{1}{\pi} \sum_n |\langle n | \hat{\mu} | \Psi(t) \rangle|^2 \frac{\eta}{(E_\Psi + \omega - E_n)^2 + \hbar^2\eta^2}. \quad (44)$$

In the limit $\eta \rightarrow 0$, we obtain the transient absorption spectrum at time t via

$$I_\mu(t, \omega) = \frac{1}{\pi} \sum_n |\langle n | \hat{\mu} | \Psi(t) \rangle|^2 \delta(E_\Psi + \omega - E_n). \quad (45)$$

It is possible to calculate the transient absorption via a direct evaluation of $\{|n\rangle\}$ by targeting the n eigenstates in the DMRG density matrix.⁸⁹ However, for a fixed number of retained DMRG density matrix eigenstates, the truncation error grows rapidly with the number of targeted states in the density matrix and thus limits the use of this approach. Hallberg,⁹⁰ and Kühner and White⁹¹ introduced the Lanczos-DMRG method which combines DMRG with the Lanczos algorithm.⁹² Lanczos-DMRG is based on the observation that it is only necessary to calculate the eigenstates that make a finite contribution to the spectrum. This is achieved by projecting the Hamiltonian \hat{H} onto a Krylov subspace spanned

by the Lanczos vectors $|f_n\rangle$.

We calculate transient spectra from the state $|\Psi(t)\rangle = |S_i\rangle$ using the Lanczos-DMRG method, with normalised Lanczos vectors defined as in ref 91, i.e.,

$$a_n = \langle f_n | \hat{H} | f_n \rangle, \quad (46)$$

$$|r_n\rangle = \left(\hat{H} - a_n \right) |f_n\rangle - b_{n-1} |f_{n-1}\rangle, \quad (47)$$

$$b_n = |||r_n\rangle||_2, \quad (48)$$

and

$$|f_{n+1}\rangle = \frac{|r_n\rangle}{b_n}, \quad (49)$$

where $b_{-1} = 0$. We require $|S_i\rangle$ to be the lowest energy eigenstate of the Hamiltonian in the projected Krylov subspace. This is achieved by projecting out the lower energy eigenstates via

$$|f_0\rangle = \left(\hat{1} - \sum_{j=0}^{i-1} |S_j\rangle \langle S_j| \right) |g_0\rangle, \quad (50)$$

where

$$|g_0\rangle = \frac{\hat{\mu} |S_i\rangle}{||\hat{\mu} |S_i\rangle||_2}. \quad (51)$$

Projecting out the eigenstates lower in energy than $|S_i\rangle$ is also motivated as we are only interested in the calculation of stimulated absorption spectra.

We now outline the implementation of Lanczos-DMRG within our adaptive tDMRG simulations. Once the dynamical simulation for time t is reached, we perform a static DMRG sweep to calculate observables, ending at the DMRG step where the system block is the same size as the environment block. We save the full Hilbert space, which is in the tDMRG basis. Then we perform a full static DMRG sweep, diagonalizing the Hamiltonian

at each DMRG step to find $|S_i\rangle$, and the Lanczos vectors $\{|f_n\rangle\}$, as defined above. The first five Lanczos vectors are used as target states during the static DMRG sweep, weighted proportionately by their contribution to the spectrum as defined by eq (17) of ref 91, i.e.,

$$w_n = \sum_m (\Phi_m^0)^2 (\Phi_m^n)^2, \quad (52)$$

where w_n is the weight of the Lanczos state n , $\Phi_m^n = \langle f_m | \Phi_n \rangle$, and $|\Phi_n\rangle$ is the n^{th} eigenstate of the Hamiltonian in the Lanczos Hilbert space. Noting that we need an accurate representation of all eigenstates up to and including $|S_i\rangle$ during the static DMRG sweep, we assign 25% of the weight to $|\Psi(t)\rangle$, 25% of the weight to all eigenstates up to $|S_i\rangle$ (distributed equally), and the remaining 50% of the weight to the target Lanczos states. At the end of the static DMRG sweep, we calculate the transient absorption spectrum using eq (45). The dynamical simulation is then continued from the saved tDMRG Hilbert space.

Lanczos-DMRG is a simple and efficient method for the calculation of the low energy discrete absorption spectra, and is well suited for a tDMRG simulation where the transient absorption is calculated as a function of time during the dynamics. More accurate, but expensive, frequency-space DMRG methods, such as correction vector DMRG⁹¹ and dynamical DMRG,⁹³ are required for the calculation of complex spectra with high energy absorptions, or continuous spectra.

6 Accuracy and convergence

The adaptive tDMRG algorithm utilized in the calculations of this paper and its companion⁵⁵ suffers from two sources of error. First, the accuracy of the DMRG algorithm is dictated by the truncation error, defined by eq (31). This error is minimized by retaining more states during the truncation. Second, the Suzuki-Trotter decomposition introduces the Trotter error which is reduced by reducing the Trotter time step, Δt . Minimizing the Trotter time step also minimizes the error associated with the use of Velocity Verlet integrator for the

nuclear dynamics.

6.1 Truncation error and entanglement entropy

Due to the variational nature of the DMRG algorithm, its accuracy can be systematically improved by increasing the number of states retained during the DMRG truncation step. Convergence of the closely related PPPP model has been extensively studied.^{24,26,52,53}

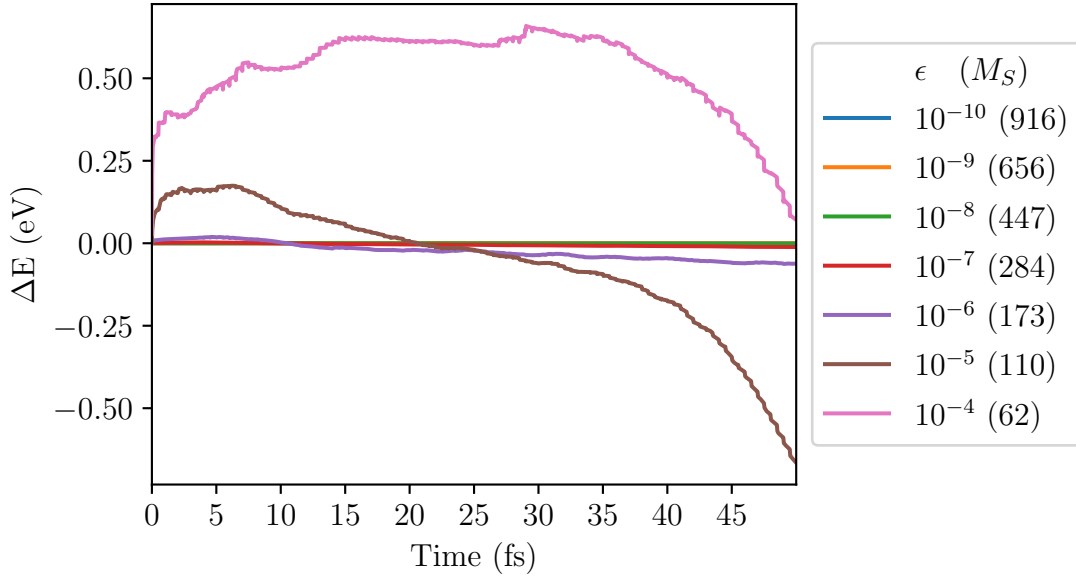


Figure 6: The calculated difference of the energy as a function of time of the system described by the evolving state vector $|\Psi(t)\rangle$ for different DMRG truncation errors, ϵ , with respect to the energy calculated with a DMRG truncation error of 10^{-11} . The maximum number of augmented block states, M_S , retained to reach the specified DMRG accuracy is indicated within parenthesis. The evolving state energy is converged for a DMRG truncation error $\epsilon = 10^{-8}$.

The convergence of the DMRG truncation error can be determined by evaluating the convergence of an observable as a function of the truncation error. As an illustrative example, Figure 6 shows the variation of energy of the evolving wavefunction $|\Psi(t)\rangle$ with the DMRG truncation error for neurosporene ($N = 18$), with $V = 3.25$ eV. The energy is converged for a truncation error of $\sim 10^{-8}$ to an accuracy of 0.1 eV.

In general, the number of states required to be retained in a DMRG scheme is given by²²

$$m \approx \exp(S), \quad (53)$$

where S is the von Neumann entanglement entropy (defined in eq (32)). For our simulations, the maximum von Neumann entanglement entropy reached, $S_{\max} < 4.0$, and thus from eq (53) the number of states required to retain $m \approx 55$. The truncation cutoff of $\sim 10^{-8}$ is reached by typically retaining ~ 400 augmented block states during the DMRG truncation, which is much larger than the number of states required by eq (53).

6.2 Trotter error

For an accurate representation of nuclear dynamics, the time step Δt should be much smaller than the timescale of nuclear motion, set by carbon-carbon bond oscillations. Typical carbon-carbon bond oscillation frequencies are ~ 20 fs, and thus we require $\Delta t < 20 \times 10^{-3}$ fs. Figure 7 illustrates the calculated expectation value of energy of the evolving wavefunction $|\Psi(t)\rangle$ as a function of Δt , for neurosporene ($N = 18$), with $V = 3.25$ eV. We notice that the energy is well converged for $\Delta t = 10^{-3}$ fs, and we use this value as the Trotter time step.

6.3 Comparison with static DMRG calculations based on Hellmann-Feynman theorem

Convergence of our program is also evaluated by comparing our dynamical results to static DMRG results obtained via the Hellmann-Feynman theorem. In the absence of the symmetry breaking term, a system prepared in $|\Psi(t=0)\rangle = |1^1B_u^+\rangle$ at the Franck-Condon point will evolve under linear damping on the $1^1B_u^+$ potential energy surface, reaching its equilibrium geometry in the long time limit. As the force on atom n , $f_n = 0$ once equilibrium is reached, the relaxed $1^1B_u^+$ state can also be found via static DMRG by setting $f_n = 0$ in eq (36) and solving the resultant equation iteratively. By comparing observables, we find that the results

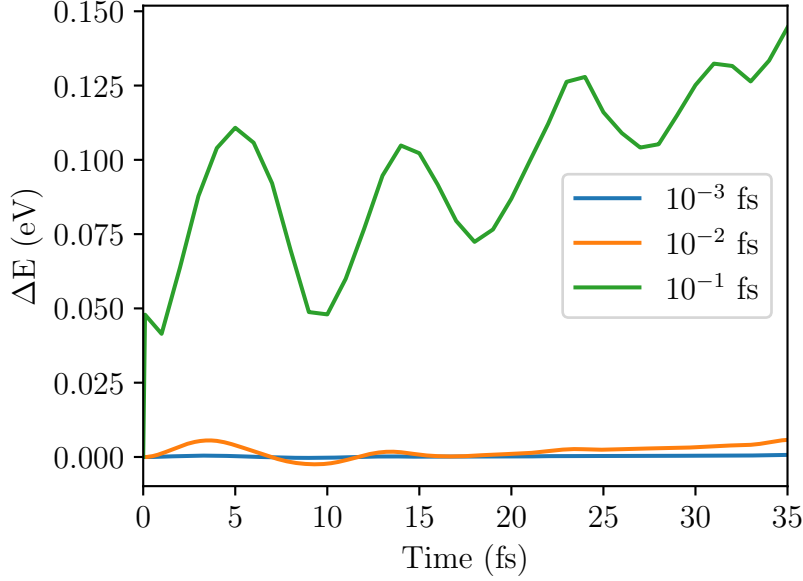


Figure 7: The calculated difference of the energy as a function of time of the system described by the evolving state vector $|\Psi(t)\rangle$ for different Trotter time steps, Δt , with respect to the energy calculated with a Trotter time step of 10^{-4} fs. Convergence is reached with a Trotter time step of 10^{-3} fs.

of our dynamic simulations converge to the same results we obtain via the self iterative Hellmann-Feynman procedure. We illustrate this convergence for the two observables of energy and staggered bond dimerizations. Figure 8 shows the staggered bond dimerizations, defined for the n^{th} bond by $\delta_n = (-1)^n(\delta u_n - \delta \bar{u}_n)/\delta \bar{u}_n$ (where $\delta u_n = u_{n+1} - u_n$ and $\delta \bar{u}_n$ is the average of δu_n over all bonds), are converged. The inset shows that the energy of the $1^1B_u^+$ state as it evolves reaches the relaxed energy calculated via the Hellmann-Feynman procedure.

6.4 Accuracy of Lanczos-DMRG calculations

The $1^1B_u^+$ state is connected to the excited states in the A_g^- sector by the dipole moment operator. Therefore, the accuracy of the Lanczos-DMRG can be evaluated by comparing the calculated transient spectra to the energies and transition dipole moments of the excited states in the A_g^- sector, calculated using static DMRG in the absence of symmetry breaking and at the vertical geometry. The results are shown in Figure 9, and demonstrate a good

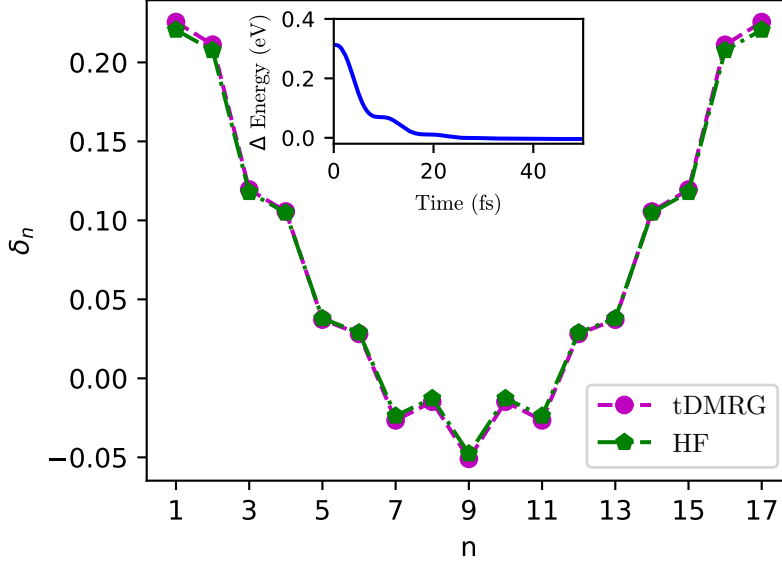


Figure 8: Staggered bond dimerizations of the relaxed $1^1B_u^+$ state calculated via tDMRG (magenta) and Hellmann-Feynman procedure (green). The inset shows the difference between the energy of the $1^1B_u^+$ state calculated via the adaptive tDMRG and the energy of the $1^1B_u^+$ state at the relaxed geometry calculated via the Hellmann-Feynman procedure, showing that the two energies converge to the same value.

agreement between the two methods.

Although targeting several Lanczos states during the static DMRG sweep of the Lanczos-DMRG procedure increases the accuracy of the calculation, it leads to a large computational expense. In our simulations, we target five Lanczos vectors, which maintains the DMRG truncation error at around $\epsilon \sim 10^{-8}$ while keeping $M_S \sim 1000$ augmented block states.

7 Approximate Two Level Dynamics

7.1 Quasi-stationary state dynamics

As observed in ref 54, for molecules possessing C_2 symmetry, the optically prepared state $|\Psi(t)\rangle$ is almost entirely composed of two adiabatic states during the entirety of the time evolution. Thus, to a good approximation, we can adopt a two-level system and express

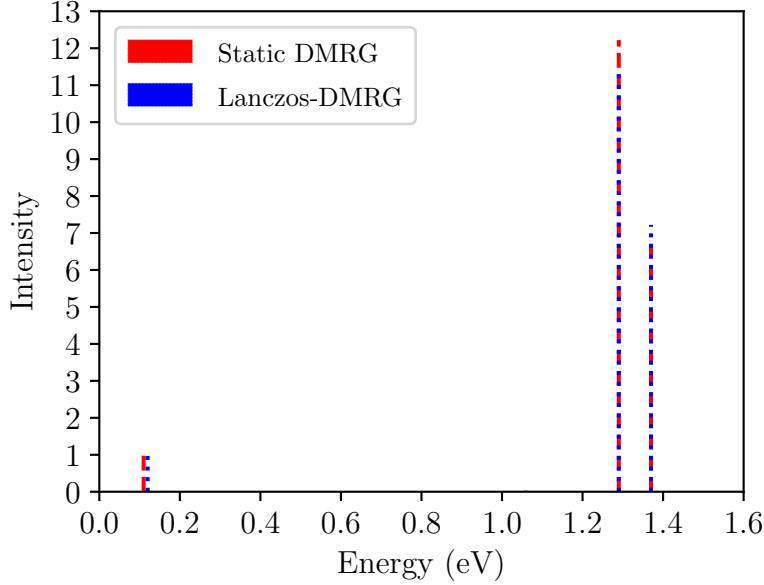


Figure 9: The transient absorption spectra calculated from the $1^1B_u^+$ state using static DMRG (red) and Lanczos-DMRG (blue). The three signals correspond to transitions to the $2^1A_g^-$, $4^1A_g^-$, and $5^1A_g^-$ states in order of increasing energy. The intensity (I) is normalized with respect to the $2^1A_g^-$ signal, i.e., $I(n^1A_g^-) = |\langle n^1A_g^- | \hat{\mu} | 1^1B_u^+ \rangle|^2 / |\langle 2^1A_g^- | \hat{\mu} | 1^1B_u^+ \rangle|^2$.

$|\Psi(t)\rangle$ as the non-stationary state

$$|\Psi(t)\rangle \approx \psi_1 |S_1\rangle \exp(-iE_1t/\hbar) + \psi_2 |S_2\rangle \exp(-iE_2t/\hbar), \quad (54)$$

where $|S_1\rangle$ and $|S_2\rangle$ are the two contributing adiabatic states, and probability amplitudes ψ_1 and ψ_2 are assumed to be constant. Denoting the two diabatic states as $|\phi_1\rangle$ and $|\phi_2\rangle$, we can write²

$$|S_1\rangle \approx a(t) |\phi_1\rangle + b(t) |\phi_2\rangle \quad (55)$$

and

$$|S_2\rangle \approx c(t) |\phi_1\rangle + d(t) |\phi_2\rangle. \quad (56)$$

²In an exact two-level system, $|a|^2 = |d|^2$ and $|c|^2 = |b|^2$.

Thus, the probability that the system occupies the diabatic state $|\phi_2\rangle$, $P(\Psi(t); \phi_2) = |\langle\phi_2|\Psi(t)\rangle|^2$, is

$$P(\Psi(t); \phi_2) = |b\psi_1|^2 + |d\psi_2|^2 + (b\psi_1)^*(d\psi_2) \cos(E_1 - E_2)t/\hbar. \quad (57)$$

Eqn. (57) describes the observed oscillatory behaviour of the diabatic probabilities of the two-level system (as shown in Figure 10(b)). Omitting the oscillatory term, we define the ‘classical’ probability of the state ϕ_2 as

$$P_{\text{classical}}(\phi_2) = |b\psi_1|^2 + |d\psi_2|^2. \quad (58)$$

7.2 Landau-Zener-like transition

In the absence of the particle-hole symmetry breaking term, \hat{H}_ϵ , a system prepared in the $1^1B_u^+$ state will remain on the same diabatic surface. In this limit, defined by $\epsilon_{\text{max}} \rightarrow 0$, the diabatic and adiabatic states are equivalent. Since the diabatic surfaces cross during the dynamical process, it implies that $|\Psi(t)\rangle$ will undergo a nonadiabatic transition while remaining in the $1^1B_u^+$ diabatic state. However, the inclusion of a non-zero \hat{H}_ϵ facilitates an adiabatic transition where the system described by $|\Psi(t)\rangle$ transforms from the $1^1B_u^+$ diabatic state to either the $1^1B_u^-$ or $2^1A_g^-$ states (i.e., negative particle-hole diabatic states) while remaining predominantly in a single adiabatic eigenstate. Figure 10 demonstrates illustrative examples of these two limits. The transition from a ‘fast’ nonadiabatic process to a ‘slow’ adiabatic process as a function of ϵ_{max} corresponds to a Landau-Zener transition.⁹⁴ In both cases, although the diabatic surfaces cross, the adiabatic surfaces exhibit an avoided crossing and not a conical intersection.

We study this transition by linearly scaling the potential energies in the symmetry breaking Hamiltonian (presented in Table 1) by a scaling factor ζ . For this system, the $|1^1B_u^+\rangle \rightarrow |2^1A_g^-\rangle$ transition is expected energetically (see Figure 2 for the diabatic vertical and relaxed excited energies). The system is prepared in $|\Psi(t=0)\rangle = |S_1\rangle$, the dipole-

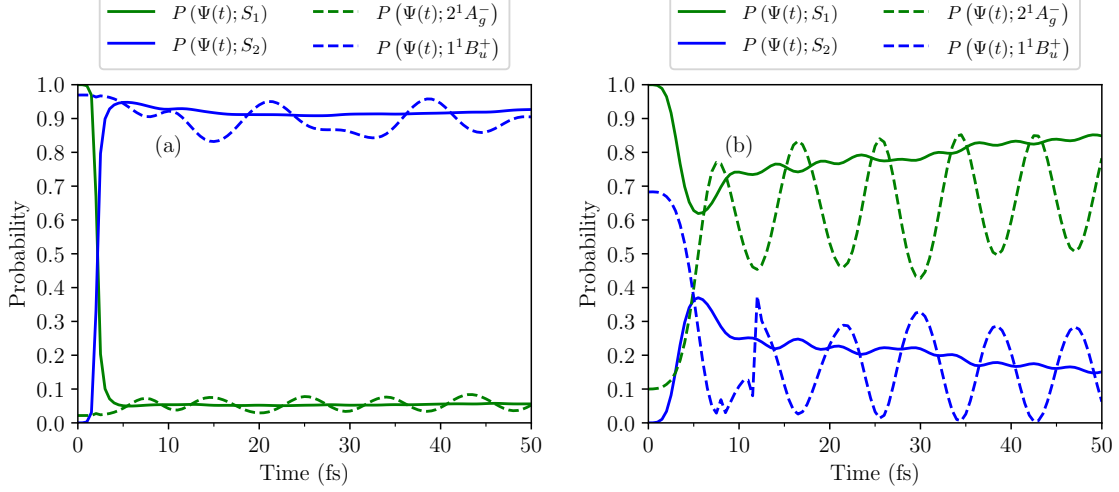


Figure 10: The probabilities as a function of time that the system described by $|\Psi(t)\rangle$ occupies the adiabatic states, S_1 and S_2 (calculated using eq (8)), and the diabatic states, $2^1A_g^-$ and $1^1B_u^+$ (calculated using eq (9)). The initial condition is that $|\Psi(0)\rangle = |S_1\rangle$. Results are for $N = 18$ and $V = 3.25$ eV, and for the symmetry breaking Hamiltonian presented in Table 1 by a linear scaling factor of (a) $\zeta = 0.2$ and (b) $\zeta = 1.2$.

allowed adiabatic excited state.

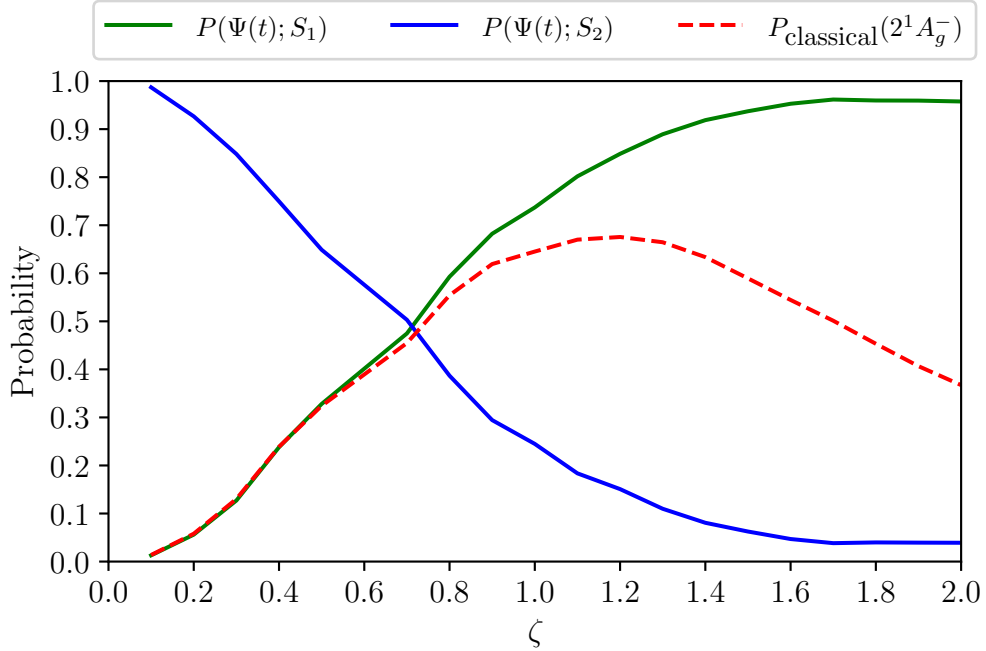


Figure 11: The probabilities at $t = 50$ fs as a function of increasing the strength of the particle-hole symmetry term (i.e., ζ) that the system described by $|\Psi(t)\rangle$ occupies the adiabatic states, S_1 and S_2 . Also shown is the classical $2^1A_g^-$ yield. The initial condition is that $|\Psi(0)\rangle = |S_1\rangle$. Results are for $N = 18$ and $V = 3.25$ eV.

Figure 11 illustrates the probabilities that the system described by $|\Psi(t)\rangle$ occupies the adiabatic excited states S_1 and S_2 at $t = 50$ fs as a function of ζ , given the initial condition that $|\Psi(t = 0)\rangle = |S_1\rangle$. As $\zeta \rightarrow 0$, $P(\Psi(t \rightarrow \infty); S_2) \rightarrow 1$ and $|S_2\rangle$ is entirely composed of $|1^1B_u^+\rangle$, as seen from Figure 10(a). Since the system is prepared with $P(\Psi(t = 0); S_1) = 1$ this corresponds to a nonadiabatic transition while staying on the $1^1B_u^+$ diabatic potential energy surface. As ζ increases, $P(\Psi(t \rightarrow \infty); S_1)$ increases and as $\zeta \rightarrow 2$, $P(\Psi(t \rightarrow \infty); S_1) \rightarrow 1$, i.e., $|\Psi(t)\rangle$ stays predominantly in $|S_1\rangle$ during the dynamics, while the probability that $|\Psi\rangle$ remains in $|1^1B_u^+\rangle$ decreases, as seen in Figure 10(b). Now the transition resembles an adiabatic process.

The ‘classical’ probability, defined by eq (58), i.e.,

$$P_{\text{classical}}(2^1A_g^-) = P(S_1; 2^1A_g^-) \times P(\Psi(t); S_1) + P(S_2; 2^1A_g^-) \times P(\Psi(t); S_2), \quad (59)$$

provides a measure of the adiabaticity of the transition. We see that as the particle-hole symmetry breaking term increases (i.e., as ζ increases), $P_{\text{classical}}$ gradually increases and reaches a maximum $\sim 65\%$ around $\zeta = 1.2$. As ζ further increases, $P(\Psi(t); 1^1B_u^+) + P(\Psi(t); 2^1A_g^-) < 1$, i.e., $|S_1\rangle$ gains contributions from higher energy diabatic states. Consequently, the process can no longer be modelled as a two-level system.

8 Conclusions

This paper has presented a dynamical simulation scheme to model the highly correlated excited state dynamics of linear polyenes. It complements our more explanatory discussion of carotenoid excited state dynamics in refs 54 and 55. We applied it to investigate the internal conversion processes of carotenoids following their photoexcitation. We use the extended Hubbard-Peierls model, \hat{H}_{UVP} , to describe the π -electronic system coupled to nuclear degrees of freedom. This is supplemented by a Hamiltonian, \hat{H}_ϵ , that explicitly breaks both the particle-hole and two-fold rotation symmetries of idealized carotenoid structures.

The electronic degrees of freedom are treated quantum mechanically by solving the time-dependent Schrödinger equation using the adaptive tDMRG method, while nuclear dynamics are treated via the Ehrenfest equations of motion. By defining adiabatic excited states as the eigenstates of the full Hamiltonian $\hat{H} = \hat{H}_{\text{UVP}} + \hat{H}_\epsilon$, and diabatic excited states as eigenstates of \hat{H}_{UVP} , we present a computational framework to monitor the internal conversion process from the initial photoexcited $1^1B_u^+$ state to the singlet triplet-pair states of carotenoids. We further incorporate Lanczos-DMRG to the tDMRG-Ehrenfest method to calculate transient absorption spectra from the evolving photoexcited state. We describe in detail the accuracy and convergence criteria for DMRG, and show that this method accurately describes the dynamical processes of carotenoid excited states. We also discuss the effect of the symmetry breaking term, \hat{H}_ϵ , on the internal conversion process, and show that its effect on the extent of internal conversion can be described by a Landau-Zener-type transition.

Mindful of the possible failures of the Ehrenfest approximation at avoided crossings (or conical intersections) described in section 4.2, future work will use the adaptive tDMRG method to simulate the excited state dynamics with fully quantized phonon degrees of freedom.

Acknowledgement

We thank Max Marcus for helpful discussions. D.M is grateful to the EPSRC Centre for Doctoral Training, Theory and Modelling in Chemical Sciences, under Grant No. EP/L015722/1 and Linacre College for a Carolyn and Franco Gianturco Scholarship and the Department of Chemistry, University of Oxford for financial support. D.J.V. received financial support from the EPSRC Centre for Doctoral Training, Theory and Modelling in Chemical Sciences (Grant ref. EP/L015722/1), the Department of Chemistry, and Balliol College Oxford via the Foley-Béjar Scholarship. We acknowledge the use of University of Oxford Advanced Research Computing (ARC) facility for this work.

References

- (1) Hudson, B. S.; Kohler, B. E. A low-lying weak transition in the polyene α,ω -diphenyloctatetraene. *Chemical Physics Letters* **1972**, *14*, 299–304.
- (2) Schulten, K.; Karplus, M. On the origin of a low-lying forbidden transition in polyenes and related molecules. *Chemical Physics Letters* **1972**, *14*, 305–309.
- (3) Pariser, R. Theory of the electronic spectra and structure of the polyacenes and of alternant hydrocarbons. *The Journal of Chemical Physics* **1956**, *24*, 250–268.
- (4) Čížek, J.; Paldus, J.; Hubač, I. Correlation effects in the low-lying excited states of the PPP models of alternant hydrocarbons. I. Qualitative rules for the effect of limited configuration interaction. *International Journal of Quantum Chemistry* **1974**, *8*, 951–970.
- (5) Szabo, A.; Langlet, J.; Malrieu, J.-P. Length dependence of excitation energies in linear polyenes: Localized and delocalized descriptions. *Chemical Physics* **1976**, *13*, 173–179.
- (6) Schulten, K.; Ohmine, I.; Karplus, M. Correlation effects in the spectra of polyenes. *The Journal of Chemical Physics* **1976**, *64*, 4422–4441.
- (7) Ohmine, I.; Karplus, M.; Schulten, K. Renormalized configuration interaction method for electron correlation in the excited states of polyenes. *The Journal of Chemical Physics* **1978**, *68*, 2298–2318.
- (8) Tavan, P.; Schulten, K. The $2^1A_g - 1^1B_u$ energy gap in the polyenes: An extended configuration interaction study. *The Journal of Chemical Physics* **1979**, *70*, 5407–5413.
- (9) Lasaga, A. C.; Aerni, R. J.; Karplus, M. Photodynamics of polyenes: The effect of electron correlation on potential surfaces. *The Journal of Chemical Physics* **1980**, *73*, 5230–5243.

- (10) Tavan, P.; Schulten, K. Electronic excitations in finite and infinite polyenes. *Phys. Rev. B* **1987**, *36*, 4337–4358.
- (11) Buenker, R. J.; Whitten, J. L. Ab Initio SCF MO and CI Studies of the Electronic States of Butadiene. *The Journal of Chemical Physics* **1968**, *49*, 5381–5387.
- (12) Hosteny, R. P.; Dunning Jr, T. H.; Gilman, R. R.; Pipano, A.; Shavitt, I. A binitio study of the π -electron states of trans-butadiene. *The Journal of Chemical Physics* **1975**, *62*, 4764–4779.
- (13) Aoyagi, M.; Osamura, Y.; Iwata, S. An MCSCF study of the low-lying states of trans-butadiene. *The Journal of Chemical Physics* **1985**, *83*, 1140–1148.
- (14) Serrano-Andrés, L.; Lindh, R.; Roos, B. O.; Merchán, M. Theoretical study of the electronic spectrum of all-trans-1,3,5,7-octatetraene. *Journal of Physical Chemistry* **1993**, *97*, 9360–9368.
- (15) Hsu, C.-P.; Hirata, S.; Head-Gordon, M. Excitation Energies from Time-Dependent Density Functional Theory for Linear Polyene Oligomers: Butadiene to Decapentaene. *The Journal of Physical Chemistry A* **2001**, *105*, 451–458.
- (16) Silva-Junior, M. R.; Schreiber, M.; Sauer, S. P. A.; Thiel, W. Benchmarks for electronically excited states: Time-dependent density functional theory and density functional theory based multireference configuration interaction. *The Journal of Chemical Physics* **2008**, *129*, 104103.
- (17) Starcke, J. H.; Wormit, M.; Schirmer, J.; Dreuw, A. How much double excitation character do the lowest excited states of linear polyenes have? *Chemical Physics* **2006**, *329*, 39–49.
- (18) Angeli, C.; Pastore, M. The lowest singlet states of octatetraene revisited. *Journal of Chemical Physics* **2011**, *134*, 184302.

- (19) Marian, C. M.; Gilka, N. Performance of the density functional theory/multireference configuration interaction method on electronic excitation of extended π -systems. *Journal of Chemical Theory and Computation* **2008**, *4*, 1501–1515.
- (20) Kleinschmidt, M.; Marian, C. M.; Waletzke, M.; Grimme, S. Parallel multireference configuration interaction calculations on mini- β -carotenes and β -carotene. *Journal of Chemical Physics* **2009**, *130*, 044708.
- (21) White, S. R. Density matrix formulation for quantum renormalization groups. *Physical Review Letters* **1992**, *69*, 2863–2866.
- (22) Feiguin, A. E. In *Strongly Correlated Systems: Numerical Methods*; Avella, A., Mancini, F., Eds.; Springer Berlin Heidelberg: Berlin, Heidelberg, 2013; pp 31–65.
- (23) Fano, G.; Ortolani, F.; Ziosi, L. The density matrix renormalization group method: Application to the PPP model of a cyclic polyene chain. *The Journal of Chemical Physics* **1998**, *108*, 9246–9252.
- (24) Bursill, R. J.; Barford, W. Electron-Lattice Relaxation, and Soliton Structures and Their Interactions in Polyenes. *Phys. Rev. Lett.* **1999**, *82*, 1514–1517.
- (25) Barford, W.; Bursill, R. J.; Lavrentiev, M. Y. Density-matrix renormalization-group calculations of excited states of linear polyenes. *Phys. Rev. B* **2001**, *63*, 195108.
- (26) Barford, W.; Bursill, R. J.; Lavrentiev, M. Y. Breakdown of the adiabatic approximation in trans-polyacetylene. *Phys. Rev. B* **2002**, *65*, 75107.
- (27) Barford, W. *Electronic and optical properties of conjugated polymers*, 2nd ed.; Oxford University Press: Oxford, 2013.
- (28) White, S. R.; Martin, R. L. Ab initio quantum chemistry using the density matrix renormalization group. *The Journal of Chemical Physics* **1999**, *110*, 4127–4130.

- (29) Ghosh, D.; Hachmann, J.; Yanai, T.; Chan, G. K. L. Orbital optimization in the density matrix renormalization group, with applications to polyenes and β -carotene. *Journal of Chemical Physics* **2008**, *128*, 144117.
- (30) Helgaker, T.; Jørgensen, P.; Olsen, J. *Molecular Electronic-Structure Theory*; John Wiley & Sons, 2014.
- (31) Wouters, S.; Van Neck, D. The density matrix renormalization group for ab initio quantum chemistry. *European Physical Journal D* **2014**, *68*, 272.
- (32) Taffet, E. J.; Lee, B. G.; Toa, Z. S. D.; Pace, N.; Rumbles, G.; Southall, J.; Cogdell, R. J.; Scholes, G. D. Carotenoid Nuclear Reorganization and Interplay of Bright and Dark Excited States. *The Journal of Physical Chemistry B* **2019**, *123*, 8628–8643.
- (33) Khokhlov, D.; Belov, A. Ab Initio Study of Low-Lying Excited States of Carotenoid-Derived Polyenes. *Journal of Physical Chemistry A* **2020**, *124*, 5790–5803.
- (34) Daley, A. J.; Kollath, C.; Schollwöck, U.; Vidal, G. Time-dependent density-matrix renormalization-group using adaptive effective Hilbert spaces. *Journal of Statistical Mechanics: Theory and Experiment* **2004**, *2004*, P04005.
- (35) White, S. R.; Feiguin, A. E. Real-time evolution using the density matrix renormalization group. *Physical Review Letters* **2004**, *93*, 076401.
- (36) Gobert, D.; Kollath, C.; Schollwöck, U.; Schütz, G. Real-time dynamics in spin-1/2 chains with adaptive time-dependent density matrix renormalization group. *Physical Review E - Statistical, Nonlinear, and Soft Matter Physics* **2005**, *71*, 036102.
- (37) Kollath, C.; Schollwöck, U.; Zwerger, W. Spin-charge separation in cold fermi gases: A real time analysis. *Physical Review Letters* **2005**, *95*, 176401.

- (38) Al-Hassanieh, K. A.; Feiguin, A. E.; Riera, J. A.; Büsser, C. A.; Dagotto, E. Adaptive time-dependent density-matrix renormalization-group technique for calculating the conductance of strongly correlated nanostructures. *Physical Review B - Condensed Matter and Materials Physics* **2006**, *73*, 195304.
- (39) Dias Da Silva, L. G.; Heidrich-Meisner, F.; Feiguin, A. E.; Büsser, C. A.; Martins, G. B.; Anda, E. V.; Dagotto, E. Transport properties and Kondo correlations in nanostructures: Time-dependent DMRG method applied to quantum dots coupled to Wilson chains. *Physical Review B - Condensed Matter and Materials Physics* **2008**, *78*, 195317.
- (40) White, S. R.; Affleck, I. Spectral function for the S=1 Heisenberg antiferromagnetic chain. *Physical Review B - Condensed Matter and Materials Physics* **2008**, *77*, 134437.
- (41) Al-Hassanieh, K. A.; Reboredo, F. A.; Feiguin, A. E.; González, I.; Dagotto, E. Excitons in the one-dimensional Hubbard model: A real-time study. *Physical Review Letters* **2008**, *100*, 166403.
- (42) Heidrich-Meisner, F.; Feiguin, A. E.; Dagotto, E. Real-time simulations of nonequilibrium transport in the single-impurity Anderson model. *Physical Review B* **2009**, *79*, 235336.
- (43) Mannouch, J. R.; Barford, W.; Al-Assam, S. Ultra-fast relaxation, decoherence, and localization of photoexcited states in π -conjugated polymers. *Journal of Chemical Physics* **2018**, *148*, 034901.
- (44) Barford, W.; Mannouch, J. R. Torsionally induced exciton localization and decoherence in π -conjugated polymers. *Journal of Chemical Physics* **2018**, *149*, 214107.
- (45) Perez, I. G.; Barford, W. Ultrafast Fluorescence Depolarization in Conjugated Polymers. *Journal of Physical Chemistry Letters* **2021**, *12*, 5344–5348.

- (46) Xie, X.; Liu, Y.; Yao, Y.; Schollwöck, U.; Liu, C.; Ma, H. Time-dependent density matrix renormalization group quantum dynamics for realistic chemical systems. *Journal of Chemical Physics* **2019**, *151*, 224101.
- (47) Schröder, F. A.; Turban, D. H.; Musser, A. J.; Hine, N. D.; Chin, A. W. Tensor network simulation of multi-environmental open quantum dynamics via machine learning and entanglement renormalisation. *Nature Communications* **2019**, *10*, 1–10.
- (48) Ren, J.; Li, W.; Jiang, T.; Wang, Y.; Shuai, Z. Time-dependent density matrix renormalization group method for quantum dynamics in complex systems. *Wiley Interdisciplinary Reviews: Computational Molecular Science* **2022**, e1614.
- (49) Chandross, M.; Mazumdar, S. Coulomb interactions and linear, nonlinear, and triplet absorption in poly(para-phenylenevinylene). *Physical Review B - Condensed Matter and Materials Physics* **1997**, *55*, 1497–1504.
- (50) Castleton, C. W.; Barford, W. Screening and the quantitative π -model description of the optical spectra and polarizations of phenyl based oligomers. *Journal of Chemical Physics* **2002**, *117*, 3570–3582.
- (51) Yaron, D.; Moore, E. E.; Shuai, Z.; Brédas, J. L. Comparison of density matrix renormalization group calculations with electron-hole models of exciton binding in conjugated polymers. *The Journal of Chemical Physics* **1998**, *108*, 7451–7458.
- (52) Bursill, R. J.; Barford, W. Large-scale numerical investigation of excited states in poly(para-phenylene). *Phys. Rev. B* **2002**, *66*, 205112.
- (53) Bursill, R. J.; Barford, W. Symmetry-adapted density matrix renormalization group calculations of the primary excited states of poly(para-phenylene vinylene). *The Journal of Chemical Physics* **2009**, *130*, 234302.

- (54) Manawadu, D.; Valentine, D. J.; Marcus, M.; Barford, W. Singlet Triplet-Pair Production and Possible Singlet-Fission in Carotenoids. *The Journal of Physical Chemistry Letters* **2022**, *13*, 1344–1349.
- (55) Manawadu, D.; Georges, T. N.; Barford, W. Photoexcited state dynamics and singlet fission in carotenoids. *Journal of Physical Chemistry A* **2023**,
- (56) Valentine, D. J.; Manawadu, D.; Barford, W. Higher energy triplet-pair states in polyenes and their role in intramolecular singlet fission. *Phys. Rev. B* **2020**, *102*, 125107.
- (57) Hashimoto, H.; Uragami, C.; Yukihiro, N.; Gardiner, A. T.; Cogdell, R. J. Understanding/unravelling carotenoid excited singlet states. *Journal of the Royal Society Interface* **2018**, *15*, 20180026.
- (58) Neese, F. The ORCA program system. *Wiley Interdisciplinary Reviews: Computational Molecular Science* **2012**, *2*, 73–78.
- (59) Neese, F. Software update: the ORCA program system, version 4.0. *Wiley Interdisciplinary Reviews: Computational Molecular Science* **2017**, *8*, 73–78.
- (60) Stephens, P. J.; Devlin F. J.; Chabalowski, C. F.; Frisch, M. J. Ab Initio Calculation of Vibrational Absorption and Circular Dichroism Spectra Using Density Functional Force Fields. *J. Phys. Chem.* **1994**, *98*, 11623.
- (61) Weigend, F.; Ahlrichs, R. Balanced basis sets of split valence, triple zeta valence and quadruple zeta valence quality for H to Rn: Design and assessment of accuracy. *Phys. Chem. Chem. Phys.* **2005**, *7*, 3297.
- (62) Weigend, F.; Ahlrichs, R. Accurate Coulomb-fitting basis sets for H to Rn. *Phys. Chem. Chem. Phys.* **2006**, *8*, 1057.
- (63) Levitin, E. S.; Polyak, B. T. Constrained minimization methods. *USSR Computational Mathematics and Mathematical Physics* **1966**, *6*, 1–50.

- (64) Schollwöck, U. The density-matrix renormalization group. *Reviews of Modern Physics* **2005**, *77*, 259–315.
- (65) White, S. R. Spin Gaps in a Frustrated Heisenberg Model for CaV_4O_9 . *Physical Review Letters* **1996**, *77*, 3633–3636.
- (66) Schollwöck, U. The density-matrix renormalization group in the age of matrix product states. *Annals of Physics* **2011**, *326*, 96–192.
- (67) Baiardi, A.; Reiher, M. The density matrix renormalization group in chemistry and molecular physics: Recent developments and new challenges. *The Journal of Chemical Physics* **2020**, *152*, 40903.
- (68) Ma, H.; Schollwöck, U.; Shuai, Z. In *Density Matrix Renormalization Group (DMRG)-based Approaches in Computational Chemistry*; Ma, H., Schollwöck, U., Shuai, Z., Eds.; Elsevier, 2022; pp 57–90.
- (69) Ma, H.; Schollwöck, U.; Shuai, Z. In *Density Matrix Renormalization Group (DMRG)-based Approaches in Computational Chemistry*; Ma, H., Schollwöck, U., Shuai, Z., Eds.; Elsevier, 2022; pp 91–147.
- (70) Schollwöck, U. Time-dependent Density-Matrix Renormalization-Group Methods. *Journal of the Physical Society of Japan* **2005**, *74*, 246–255.
- (71) Vidal, G. Efficient classical simulation of slightly entangled quantum computations. *Physical Review Letters* **2003**, *91*, 147902.
- (72) Vidal, G. Efficient simulation of one-dimensional quantum many-body systems. *Physical Review Letters* **2004**, *93*, 040502.
- (73) Eisert, J.; Cramer, M.; Plenio, M. B. Colloquium: Area laws for the entanglement entropy. *Reviews of modern physics* **2010**, *82*, 277.

- (74) Hastings, M. B. An area law for one-dimensional quantum systems. *Journal of statistical mechanics: theory and experiment* **2007**, *2007*, P08024.
- (75) Tully, J. C. *Modern Methods for Multidimensional Dynamics Computations in Chemistry*; 1998; pp 34–72.
- (76) Valentine, D. Singlet fission in linear π -conjugated systems. Ph.D. thesis, University of Oxford, 2020.
- (77) Porter, R. N.; Raff, L. M. In *Dynamics of Molecular Collisions: Part B*; Miller, W. H., Ed.; Springer US: Boston, MA, 1976; pp 1–52.
- (78) Allen, M. P.; Tildesley, D. J. *Computer simulation of liquids*; Oxford university press, 2017.
- (79) Karplus, M.; Petsko, G. A. Molecular dynamics simulations in biology. *Nature* **1990**, *347*, 631–639.
- (80) Micha, D. A. A self-consistent eikonal treatment of electronic transitions in molecular collisions. *The Journal of Chemical Physics* **1982**, *78*, 7138–7145.
- (81) Sawada, S. I.; Nitzan, A.; Metiu, H. Mean-trajectory approximation for charge- and energy-transfer processes at surfaces. *Physical Review B* **1985**, *32*, 851–867.
- (82) Head-Gordon, M.; Tully, J. C. Molecular dynamics with electronic frictions. *The Journal of Chemical Physics* **1995**, *103*, 10137–10145.
- (83) Bała, P.; Grochowski, P.; Lesyng, B.; McCammon, J. A. Quantum-classical molecular dynamics simulations of proton transfer processes in molecular complexes and in enzymes. *Journal of Physical Chemistry* **1996**, *100*, 2535–2545.
- (84) Andrade, X.; Castro, A.; Zueco, D.; Alonso, J. L.; Echenique, P.; Falceto, F.; Rubio, Á. Modified ehrenfest formalism for efficient large-scale ab initio molecular dynamics. *Journal of Chemical Theory and Computation* **2009**, *5*, 728–742.

- (85) Tully, J. C.; Preston, R. K. Trajectory surface hopping approach to nonadiabatic molecular collisions: The reaction of H^+ with D_2 . *The Journal of Chemical Physics* **1971**, *55*, 562–572.
- (86) Mannouch, J. Exciton Dynamics in π -Conjugated Polymer Systems. Ph.D. thesis, University of Oxford, 2019.
- (87) Berera, R.; van Grondelle, R.; Kennis, J. T. Ultrafast transient absorption spectroscopy: Principles and application to photosynthetic systems. *Photosynthesis Research* **2009**, *101*, 105–118.
- (88) Jeckelmann, E.; Benthien, H. *Computational Many-Particle Physics*; Springer, 2008; pp 621–635.
- (89) Jeckelmann, E.; Fehske, H. Exact numerical methods for electron-phonon problems. *La Rivista del Nuovo Cimento* **2007**, *30*, 259–292.
- (90) Hallberg, K. A. Density-matrix algorithm for the calculation of dynamical properties of low-dimensional systems. *Phys. Rev. B* **1995**, *52*, R9827–R9830.
- (91) Kühner, T. D.; White, S. R. Dynamical correlation functions using the density matrix renormalization group. *Physical Review B - Condensed Matter and Materials Physics* **1999**, *60*, 335–343.
- (92) Gagliano, E. R.; Balseiro, C. A. Dynamical Properties of Quantum Many-Body Systems at Zero Temperature. *Phys. Rev. Lett.* **1987**, *59*, 2999–3002.
- (93) Jeckelmann, E. Dynamical density-matrix renormalization-group method. *Physical Review B - Condensed Matter and Materials Physics* **2002**, *66*, 045114.
- (94) Zener, C. Non-adiabatic crossing of energy levels. *Proceedings of the Royal Society of London. Series A, Containing Papers of a Mathematical and Physical Character* **1932**, *137*, 696–702.

Graphical TOC Entry

